Available online at www.sciencedirect.com

ScienceDirect

Advances in Space Research 75 (2025) 3692–3704

ADVANCES IN SPACE RESEARCH (a COSPAR publication)

www.elsevier.com/locate/asr

Remotely sensed atmospheric anomalies of the 2022 Mw 7.0 Bantay, Philippines earthquake

Sohrab Khan [a], Munawar Shah [a,*], Punyawi Jamjareegulgarn [b], Ahmed M. El-Sherbeeny [c], Mostafa R. Abukhadra [d,e], Majid Khan [f]

[a] *Space Education and GNSS lab, National Center of GIS and Space Application, Department of Space Science, Institute of Space Technology, Islamabad 44000, Pakistan*

[b] *King Mongkut's Institute of Technology Ladkrabang, Prince of Chumphon Campus, Chumphon 86160, Thailand*

[c] *Industrial Engineering Department, College of Engineering, King Saud University, P.O. Box 800, Riyadh 11421, Saudi Arabia*

[d] *Geology Department, Faculty of Science, Beni-Suef University, Beni Suef City, Egypt*

[e] *Materials Technologies and Their Applications Lab, Faculty of Science, Beni-Suef University, Beni Suef City, Egypt*

[f] *School of Civil and Resources Engineering, University of Science and Technology Beijing, 100083 Beijing, China*

Received 26 July 2024; received in revised form 3 December 2024; accepted 5 December 2024
Available online 9 December 2024

Abstract

Remote sensing satellites have emerged as invaluable tools for surveilling natural disasters with more inevitable insights at various altitudes in atmosphere for various precursors. Moreover, the methods and satellite data before and after any event need more understanding for predicting the main shock due to the complexity of precursors. This study involves data from multiple sensors to assess how atmospheric parameters change in space and time over the Mw 7.0 Bantay, Philippines epicenter. The methods of statistical analysis, Nonlinear Autoregressive Network with Exogenous Inputs (NARX), and Multilayer Perceptron (MLP) are applied to various atmospheric parameters, including Land Surface Temperature (LST), Air Temperature (AT), Relative Humidity (RH), and Outgoing Longwave Radiation (OLR) to identify abnormal atmospheric patterns associated with earthquakes (EQ). These analyses focus on 3–5 days before the earthquake day. For this purpose, we trained daily average indices of atmospheric parameters for the month leading up to and the 15 days following the main shock. Since variations are irregular, detection can be challenging with classical statistics; therefore, we leveraged supervised machine learning to detect anomalies promptly and minimize the chances of missed detection. Thus, these findings support the lithosphere-atmosphere–ionosphere coupling (LAIC) hypothesis and suggest the need for further investigation in future research.

Keywords: Remote sensing; Earthquakes; Atmosphere; Coupling

1. Introduction

Earthquakes (EQs) occur due to crustal fractures triggered by the unusual buildup of energy beneath the lithosphere, resulting in profound damage to infrastructure and loss of life. This unusual energy occurs during tectonic stress periods, leading to brittle failures on the lithosphere (Draz et al., 2024). It has been recorded that anomalies linked with EQs can be detected not only by the ground stations but also by satellites within the atmosphere during the seismic preparation period (Liu et al., 2004; Pulinets

* Corresponding author.
E-mail address: munawar0907@hotmail.com (M. Shah).

https://doi.org/10.1016/j.asr.2024.12.013

and Dunajecka, 2007; Kuo et al., 2014). The satellite measurements have been evaluated to distinguish precursors of EQ from the Earth observation missions. The Global Navigation and Satellite System (GNSS) and Remote Sensing (RS) satellites are on the verge of sensing seismic energy remotely at various altitudes with the incursion of state-of-the-art methods (Blackett et al., 2011; Heki, 2011; Carter et al., 2013; Shah and Jin, 2015; Shah et al., 2021; Shah et al., 2022). However, there haven't been any legitimate EQ anomalies identified despite some low-magnitude anomalies both before (ranging from 2-20 days prior) and after (within 10 days) the EQ day. Interestingly, these anomalies occur not only on the surface but also in the atmosphere and show deviation of the applied constraints as negative and positive values (Eshkuvatov et al., 2024).

To put it in perspective, the ground-based stations for monitoring the EQs are few as compared to satellite-based surveillance stations dedicated to monitoring EQ. In recent times, EQ research has made significant by utilizing thermal RS with detail datasets that capture changes over the time (Hafeez et al., 2022; Hafeez et al., 2021). Depending on the altitude near the epicenter and the timing of significant EQs, the precursors can be categorized into three types. The first type can be noticed on the surface as LST, followed by the irregularities in atmosphere by RH, AT, and OLR. The third type is the ionospheric perturbations in the form of electron density, total electron content, and plasma temperature (Shah and Jin, 2018).

Many reports primarily focused on energy evolution before the EQs as thermal anomalies, as they could potentially serve as precursors. For example, satellite parameters such as LST and OLR were identified to offer abrupt increases associated with the main shocks (Hafeez et al., 2022; Zhang et al., 2023a; Ma et al., 2024; Tian et al., 2024). A relationship exists between the formation of thermal infrared anomalies and their interaction with the atmosphere, driven by seismic activity and the release of radon gas due to tectonic stress (Pulinets and Ouzounov, 2011). In the atmosphere, the decay of radon ionizes the air, leading to a rise in surface temperature and a drop in humidity at the Earth-atmosphere interface, ultimately drifting the atmosphere upward (Adil et al., 2021a). The tectonic plate movement further enhances immense pressure at deep underground during an EQ preparation period within a few kilometers to several kilometers at hypocentral depth, and this pressure can rupture the rocks. As a result, seismic waves are propagated to the surface of the Earth and significant amounts of energy are accompanied by these surface waves (Hafeez et al., 2022; Sun et al., 2024). Before an EQ, thermal activity on the land surface is hypothesized to be stimulated by pressure within the rocks triggering a temperature rise. Thermal Infrared (TIR) waves are believed to be generated due to stress buildup, leading to an escalation in thermal activity over epicenters (Ouzounov and Freund, 2004). Recent studies indicate that advanced machine learning techniques can promptly model these complex patterns as possible EQ precursors. Moreover, various ML methods can be implemented for modeling the signals like ensembles (Decision Trees, Bagging, Boosting, and Random Forests), Optimization Algorithms, and Artificial Neural Networks (ANN) (Shah et al., 2018 Geller, 1997; Pulinets and Ouzounov, 2011; Deb et al., 2016; D'Alessandro et al., 2020; Salikhov et al., 2022; Adil et al., 2021a; Freund et al., 2021; Jiao and Shan, 2022). The utilization of ML analysis for predicting atmospheric parameters or anomalies holds immense significance in enhancing our understanding of the Earth system dynamics and improving early warning systems for natural disasters. By leveraging the power of ML techniques, we can extract valuable insights from complex datasets by enabling more accurate and timely predictions of atmospheric phenomena and the EQ (Akhoondzadeh, 2013b; Shah et al., 2018).

In this study, we investigated potential atmospheric anomalies linked to the Mw 7.0 Philippines EQ. Previous studies have used total electron content as a key parameter to detect EQ. However, since GNSS stations can sometimes fail to provide data within the seismogenic zone, this paper aims to explore the potential of atmospheric parameters to detect EQ promptly. We used statistical methods and ML techniques (MLP and NARX) on RS data to distinguish LST, RH, OLR, and AT precursors associated with the main shock. Additionally, further analyses are conducted to understand the impact of EQs on the atmosphere. The primary goals of this paper are to identify significant time windows for co-located EQ precursors on the surface and in the atmosphere and to confirm seismic-induced atmospheric anomalies using statistical and ML techniques. This research is significant as it illuminates the intrinsic relationship between seismic activities and atmospheric phenomena by offering insights into potential precursory signals in the atmosphere. Understanding these dynamics could contribute to early warning systems and enhanced disaster preparedness strategies, thus mitigating the impact of seismic events on human lives and infrastructure (see Tables 1–3).

2. Study area

This study examines the temporal changes observed by various satellites associated with the Mw 7.0 Philippines EQ. This EQ occurred on July 27, 2022, at 00:43:26.871 (UTC) with a magnitude of 7.0 in the northwest region of Luzon in the Philippines. Due to oblique reverse faulting, the rupture originated approximately 10 km beneath the surface. The initial assessments indicate that the fault's orientation was either northward or southwestward (Fig. 1). For further details and additional information about this EQ is available on the United States Geological Survey (USGS) (https://earthquake.usgs.gov/earthquakes/eventpage/us6000i5rd/executive).

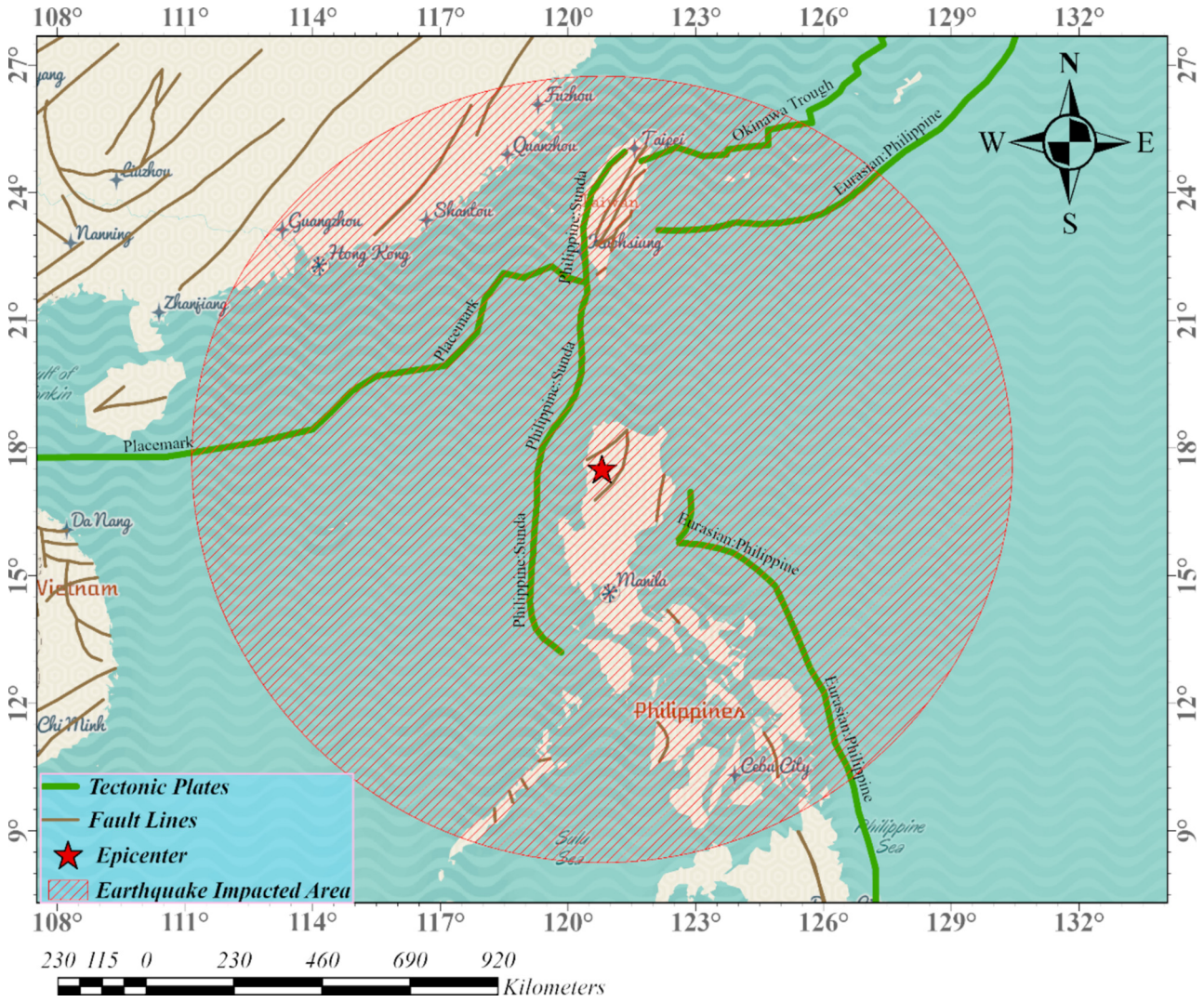

Fig. 1. The geographical map illustrates the location of the 2022 Mw 7.0 Philippines EQ with a depth of 33.7 km. The epicenter is represented by a filled red-colored star positioned at Latitude 17.6° N and Longitude 120.9° E. Major fault lines in the Luzon region are delineated on the map for reference. Moreover, the Dobrovolsky region is highlighted with a red circle.

3. Material and methodology

3.1. Datasets

In this study, we investigated EQ anomalies on surface and atmospheric indices for both the daytime and nighttime over the epicenter of the Philippines event for a time period of 45 days (30 days preceding and 15 days). Additionally, LST images are retrieved from the Terra Satellite Moderate Resolution Imaging Spectroradiometer (MODIS). Furthermore, the satellite orbits over the equator of the Earth at approximately 10:30 AM local time and is equipped with MODIS as one of its sensors; it has a bi-day revisit global orbits. MODIS can capture imagery across 36 spectral bands spanning the electromagnetic spectrum ranging from 0.415 μm to 14.235 μm in bandwidth (Tian et al., 2023; Xie et al., 2023a; Zhao et al., 2024a; Zhou et al., 2022a; Qasim et al., 2024). The detail methodological is given in the flowchart (Fig. 2). The AIRS sensor (Air Quality Sensor) is a sophisticated device designed to monitor and analyze various air quality indicators, including pollutants like carbon dioxide, ozone, and particulate matter (PM2.5 and PM10).

For this study, we retrieved the daily time-series area-averaged data of RH, AT, and OLR at a spatial resolution of 1° from the Atmospheric Infrared Sounder (AIRS)/Aqua from GIOVANNI via (https://giovanni.gsfc.nasa.gov/giovanni/). The approach of analyzing RH data is predominantly employed in studying global energy balances, atmospheric dynamics, the correlation between EQs and climate change, and the exchange between the troposphere and stratosphere at EQ epicenters. The AT is measured in Kelvin (K) to comprehend the atmospheric phenomena linked to main seismic events by analyzing the air tempera-

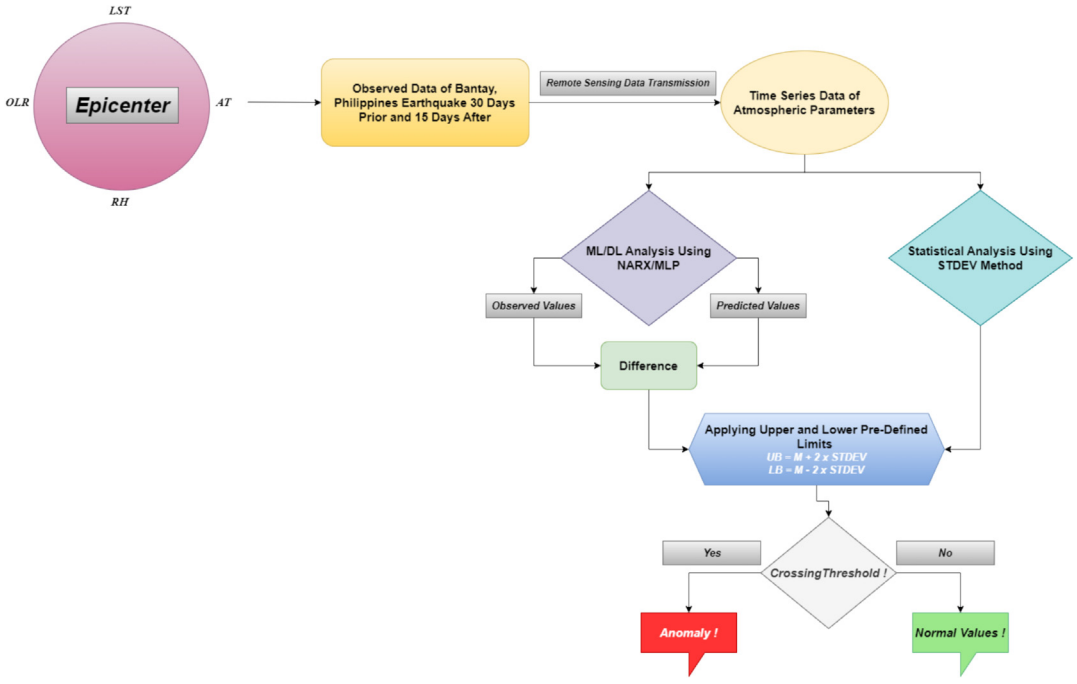

Fig. 2. The methodology for this study in the form of a flow chart.

ture's reaction to seismic activity within the atmosphere. Furthermore, the Earth's radiant climate is characterized by OLR (W/m2) as emissions emitted by clouds, the lower atmosphere, and the ground (Zhu et al., 2022).

Daily LST (°C) images obtained from the MODIS were utilized for this analysis to validate the anomalies associated with the seismic zone. During a satellite's nadir phase, MODIS LST images possess a spatial resolution of one kilometer per band for each of the three infrared wavelengths (Du & Wang, 2014; Shah et al., 2018; Zhou et al., 2022b; Chen et al., 2024; Zhao et al., 2024). In this study, we examined the MOD11A1 (V6) LST images obtained from the USGS Earth Explorer for the same 45-day time period (Xu, et al., 2022).

3.2. Methodology

A preparation zone of the epicenter is employed to estimate the atmospheric parameters retrieved for the Philippines EQ by the Dobrovolsky method, restricting the preparation zone to a specific region. This region is thought to be highly likely to detect potential precursory seismic anomalies (Dobrovolsky et al., 1979).

$$R = 10^{0.43Mw} \tag{1}$$

Moreover, the magnitude (Mw) of the EQ influences the radius (R) of the preparation zone and the larger magnitude EQs result in large stress zones, and vice versa. According to the Dobrovolsky formula, the calculated radius of the Philippines EQ is approximately 1023 km. The methodology is given in below Fig. 2.

3.2.1. Incorporating neural networks

Neural networks (NN) commonly represent intelligent systems' capacity to know intricate functional relationships from data to detect patterns. If the underlying laws governing the series are complex or unknown, NNs can capture the autocorrelation structure. The weights of network connections are primarily established by the number of weighted connections within the processing units, which are determined through training. Whenever the prediction errors surpass a predefined threshold, the main shock triggers the irregular pattern detected (Hafeez et al., 2022). Although, we have used basic statistical methods to detect anomalies in some cases, these methods fail, resulting in false positives or negatives. The use of NARX and MLP allows us to reduce missed detection and false alarms up to a greater extent due to information extracted from previous events.

3.2.2. NARX

The NARX model is employed to validate multiple anomalous atmospheric parameters. For this analysis, the datasets are divided in training, validation, and testing categories with 70 % of the data used for training, 15 % for validation, and 15 % for testing. Nonlinear time series are typically modeled using NARX equations as follows (Qasim et al., 2024; Nekoee et al., 2020):

$$y(t) = f\big(y(t-1), y(t-2), .., y\big(t-n_y\big), x(t-1), x(t-2), .., x(t-n_x)\big) \tag{2}$$

The function f is a nonlinear function. The training set comprises N observations ($y1$, $y2$, …, yN). The test set comprises the remaining observations ($yN + 1$, $yN + 2$,

..., $yN + m$). Additionally, the input layer consisted of six nodes, the hidden layer contained ten nodes, and the output layer contained one node. For this study, the neural network's input layer comprised processed data, corresponding times, and parameter deviations from the mean confidence bounds of atmospheric datasets. However, the output layer consisted of a series of daily data corresponding to the earthquake precursors. Below are the training patterns for the networks.

$$y_4 = f(y_1, y_2, y_3, t_1, t_2, t_3) \tag{3}$$

$$y_5 = f(y_2, y_3, y_4, t_2, t_3, t_4) \tag{4}$$

$$y_N = f(y_{N-3}, y_{N-2}, y_{N-1}, t_{N-3}, t_{N-2}, t_{N-1}) \tag{5}$$

To evaluate prediction performance, optimal weights are determined to minimize prediction error (PE). The PE equation can be expressed as follows:

$$PE = \sum_{k-0}^{N} (\hat{y}(t-k) - y(t-k)) \tag{6}$$

Where $\hat{y}$ represent the output of the network. The testing pattern are:

$$y_{N+4} = f\left(y_{N+1}, y_{N+2}, y_{N+3}, t_{N+1}, t_{N+2}, t_{N+3}\right) \tag{7}$$

$$y_{N+5} = f\left(y_{N+2}, y_{N+3}, y_{N+4}, t_{N+2}, t_{N+3}, t_{N+4}\right) \tag{8}$$

$$y_{N+m} = f\left(y_{N+m-3}, y_{N+m-2}, y_{N+m-1}, t_{N+m-3}, t_{N+m-2}, t_{N+m-1}\right) \tag{9}$$

To ascertain the deviations, we analyzed the differences between the actual values and the expected values (Khan et al., 2022). Moreover, the maximum deviation displayed the anomalous behavior exhibited by the observed parameters.

3.2.3. MLP

To observe the atmospheric parameters' abrupt variations, we employed the MLP model. This model comprises of three layers: an input layer with n input bits, a hidden layer with hidden units, and an output layer with a single output bit (Qasim et al., 2024; Tian et al., 2019). It is vital to note that the hidden layer nodes are connected to both the inputs and outputs, making them an essential part of the model. The datasets are split into two sets for anomaly detection based on training and testing patterns. A model-measured value is deemed anomalous if the prediction error (PE) extends beyond the bounds of the model. This possessed the construction the neural network (NN) and calculating the PE of the model. Nevertheless, despite its limitations, the Tan sigmoid function yielded the most optimal results for detecting anomalies in the output layer. Additionally, all hidden nodes are connected via the following equation (Akhoondzadeh, 2013b):

$$F(x) = \frac{2}{1 - e^{-2z}} - 1 \tag{10}$$

A Levenberg–Marquardt training algorithm is employed. A prediction process is implemented by selecting N observations, including $y_1, y_2, \ldots, y_N$ and $y_{N+1}, y_{N+2}, \ldots, y_{N+m}$, as training and test sets, respectively. For this analysis, the neural network architecture consists of three nodes in the input layer, two in the hidden layer, and only one in the output layer, respectively (Akhoondzadeh, 2013a; Hafeez et al., 2022). The proposed pattern is given below.

$$X_4 = f(x_1, x_2, x_3) \tag{11}$$

$$X_5 = f(x_2, x_3, x_4) \tag{12}$$

$$X_N = f(X_{N-3}, X_{N-2}, X_{N-1}) \tag{13}$$

Throughout the training process, the connection weights are adjusted to minimize the PE. PE equation can be expressed as follows:

$$PE = \sum_{i=4}^{N} X_i - \widehat{X}_i \tag{14}$$

$\widehat{X}_i$ is the network's output.

Pattern for testing are:

$$X_{N+4} = f(X_{N+1}, X_{N+2}, X_{N+3}) \tag{15}$$

$$X_{N+5} = f(X_{N+2}, X_{N+3}, X_{N+4}) \tag{16}$$

$$X_{N+m} = f(X_{N+m-3}, X_{N+m-2}, X_{N+m-1}) \tag{17}$$

During the testing process, any difference (DXi) among the observed (Xi) and forecasted ($\hat{X}$_i) values that exceeds the pre-defined bounds is considered an anomaly.

3.2.4. Incorporating statistical analysis into the detection of anomalies

We implemented the outlier's detection based on mean (M) and standard deviation (STDEV) to identify the possible deviations in atmospheric values associated with the seismic event. The lower (LB) and upper (UB) confidence bounds were established by comparing the M and STDEV of all the values before and after the main shock by the below equations (Draz et al., 2023). The anomaly detection method works based on the three-sigma rule where the data exceeding the three-sigma means a potential outlier and hence an anomaly.

$$UB = M + 1.6 \times (STDEV) \tag{18}$$

$$LB = M - 1.6 \times (STDEV) \tag{19}$$

The clarification in the preceding equations refers to the calculated values that fall beyond these bounds as abnormal seismic values.

4. Results

In this paper, statistical and machine learning methods monitor the abnormal atmospheric values to distinguish from various atmospheric biases onboard different satellites before and after the Philippines EQ. The resulting anomalies are below in detailed.

4.1. Air temperature

We examined the AT values for the Philippines EQ and detect a distinct positive anomaly on the third day (July 24, 2022) preceding the main event. All these parameters exhibit variations within a 5-day window preceding the major event. There was a notable rise in AT of approximately 4 K beyond the upper bound on July 24, 2022 during the daytime. Similarly, there was also an increment of 2.37 K from the upper bound during nighttime on the exact day (Fig. 3). Furthermore, we analyzed the AT values using both the NARX and MLP. With NARX, we observed an anomalous increase of 5.48 K during the daytime on July 24, 2022. Similarly, a rise of 1.86 K was observed on July 23, 2022, followed by a decrease of −1.79 K on July 24, 2022 in the nighttime values. The MLP also identified an increase in AT of 5.71 K and 3.22 K during the daytime and nighttime, respectively. Moreover, employing various techniques to analyze the AT values during both the day and nighttime reveals a significant thermal anomaly on July 24, 2022, three days prior to the major event.

4.2. Relative humidity

In this paper, the RH datasets showed deviations over the epicenter to designate anomalies of the main event. The statistical observation of RH during the daytime shows a decrease of −3.04 % from the lower bound within three days before the main event on July 24, 2022. Similarly, the decrease in RH was −0.9 % on the same day during nighttime. We also observed a precursory value in RH by both the NARX and MLP by a noticeable negative anomaly before the event on the same day. The NARX predicted decrease in daytime RH was −6.48 % (Fig. 4b), while during the nighttime, the decrease was −4.64 % (Fig. 4f). The MLP predicted RH value during the day time

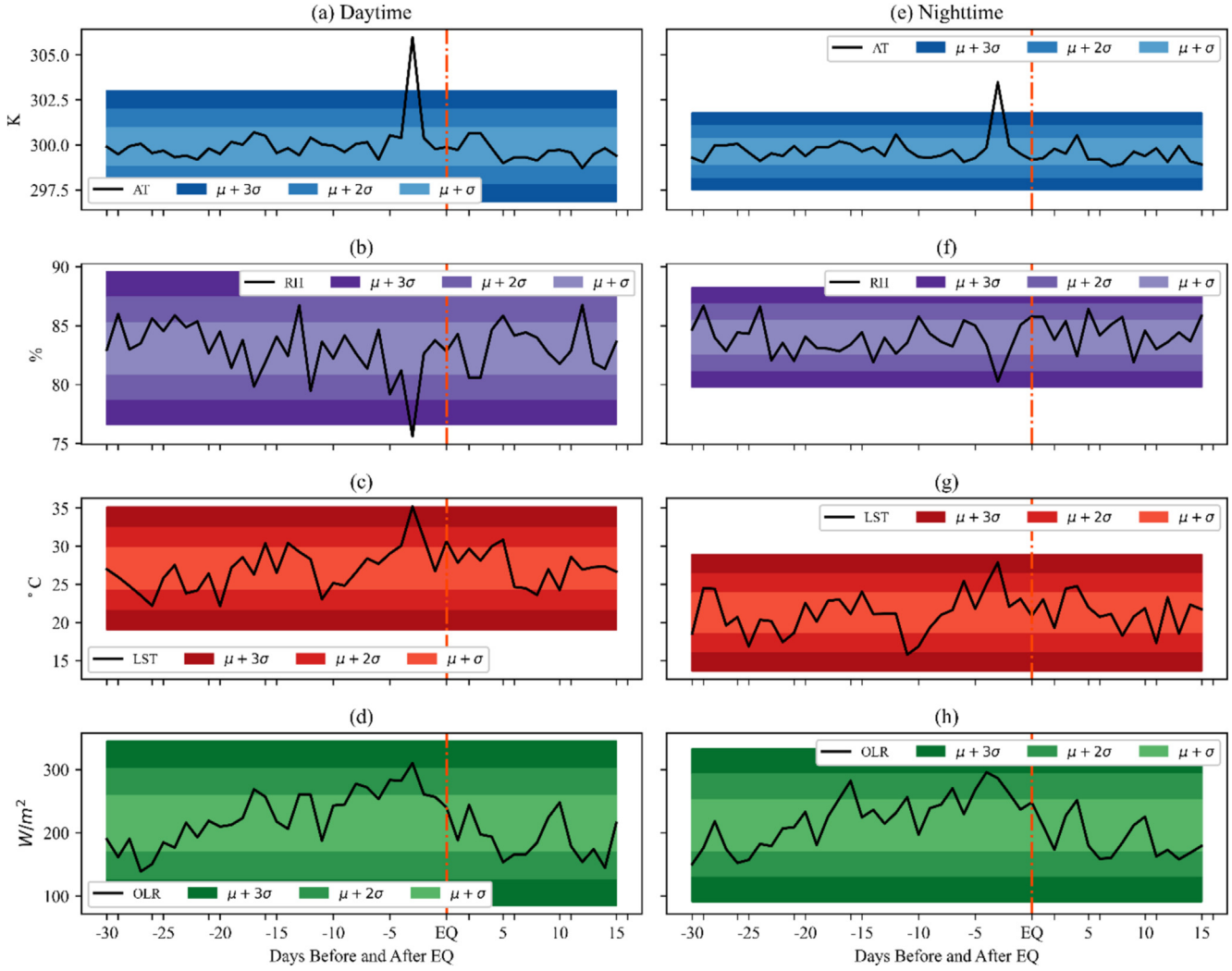

Fig. 3. The illustration of the statistical analysis of day and nighttime values in diurnal variations. (a) AT data with upper and lower bounds, b) daytime RH averaged, (c) daytime LST averaged, (d) daytime OLR averaged data with bounds, (e) nighttime AT averaged, (f) nighttime RH averaged, (g) nighttime LST averaged, (h) nighttime averaged OLR with confidence bounds. The red dashed line indicates the EQ.

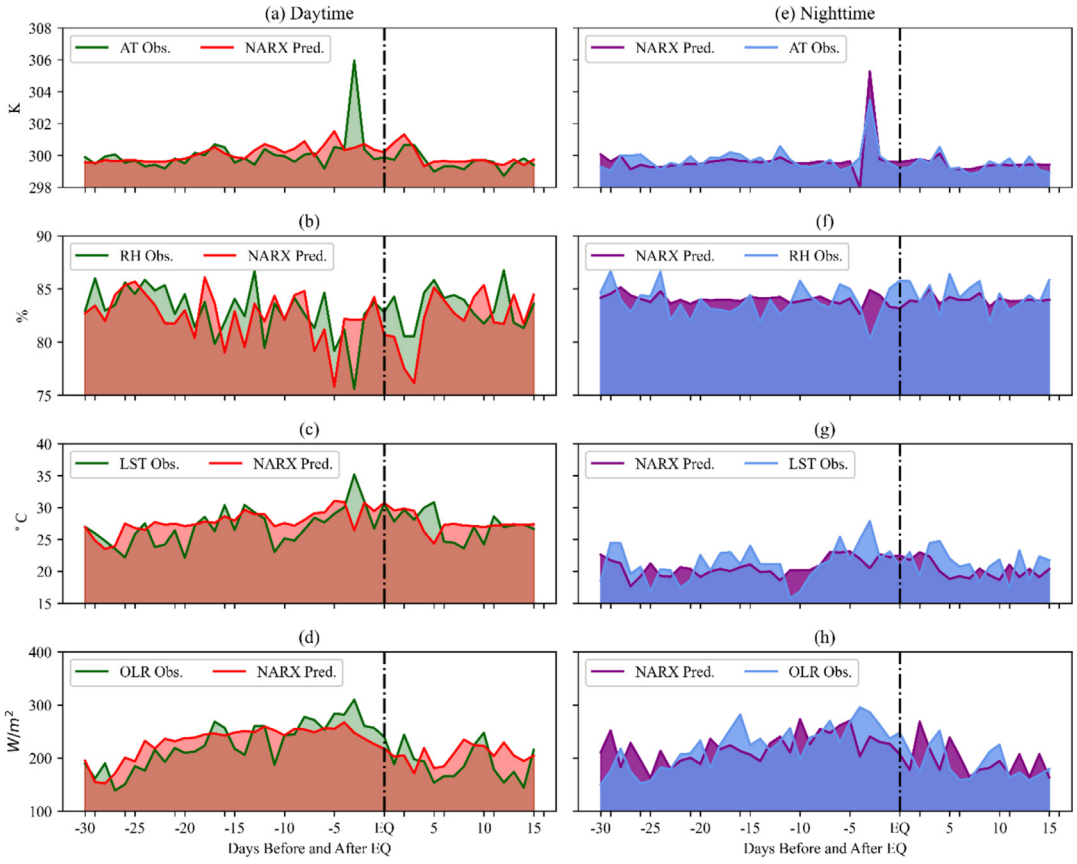

Fig. 4. The illustration of the NARX analysis of daytime and nighttime values. (a) AT daytime data observed and forecasted, (b) RH daytime data observed and forecasted, (c) LST daytime data observed and forecasted, (d) OLR daytime data observed and forecasted, (e) AT daytime data observed and forecasted, (f) RH daytime data observed and forecasted, (g) LST daytime data observed and forecasted, (h) OLR daytime data observed and forecasted. The black dashed line is for the EQ-day.

was −5.797 % (Fig. 5b), also indicating a clear negative anomaly before the main shock and the MLP predicted decrease was −2.96 % (Fig. 5f) on the same day during the nighttime.

4.3. Land surface temperature

The EQ anomalies are also investigated in the diurnal MODIS LST of the Philippines EQ for both the daytime and nighttime. By implementing statistical analysis, we observed an anomalous rise of 2.76 °C in the daytime and 2.22 °C in the nighttime (Fig. 5). Similarly, a daytime anomaly of 8.75 °C is evident on July 24 using NARX, while another daytime variation of 6.48 °C is observed five days after the main event. During the nighttime, the anomaly is 7.39 °C (Liu et al., 2021). Moreover, Fig. 5 clearly illustrates a daytime anomaly of 4.92 °C using MLP, along with a nighttime anomaly of 5.01 °C.

4.4. Outgoing longwave radiation

The daytime OLR values exhibited a positive anomaly of 8.87 W/m^2 on 3rd day before the main shock on July 24, 2022. Similarly, the nighttime OLR values showed a positive deviation from the upper bound of 3.38 W/m^2 on the same day. The NARX and MLP analyses during the daytime and nighttime also demonstrated significant variations. The NARX-predicted OLR value was 62.58 W/m^2 during the daytime on July 24, 2022, while during the nighttime, the predicted value was 92.25 W/m^2. Similarly, the predicted value by MLP was 79.54 W/m^2 during the daytime, whereas the predicted value during the nighttime was 100.34 W/m^2 four days before on July 23, 2022. Moreover, both the statistical analysis and the predictions by NARX and MLP indicated a positive anomaly within the 5-day window before the major event (Figs. 6 and 7).

5. Discussion

This study employed a combined statistical and ML approaches to examine potential earthquake precursors of the Philippine EQ. In previous and related studies, it can be observed that ionosphere and total electron content (TEC) are taken as the main signals for seismic-ionospheric anomaly detection. Whereas, the TEC data can sometimes be unavailable due to various issues. So, in this study, we relied on the atmospheric parameters to study the effect

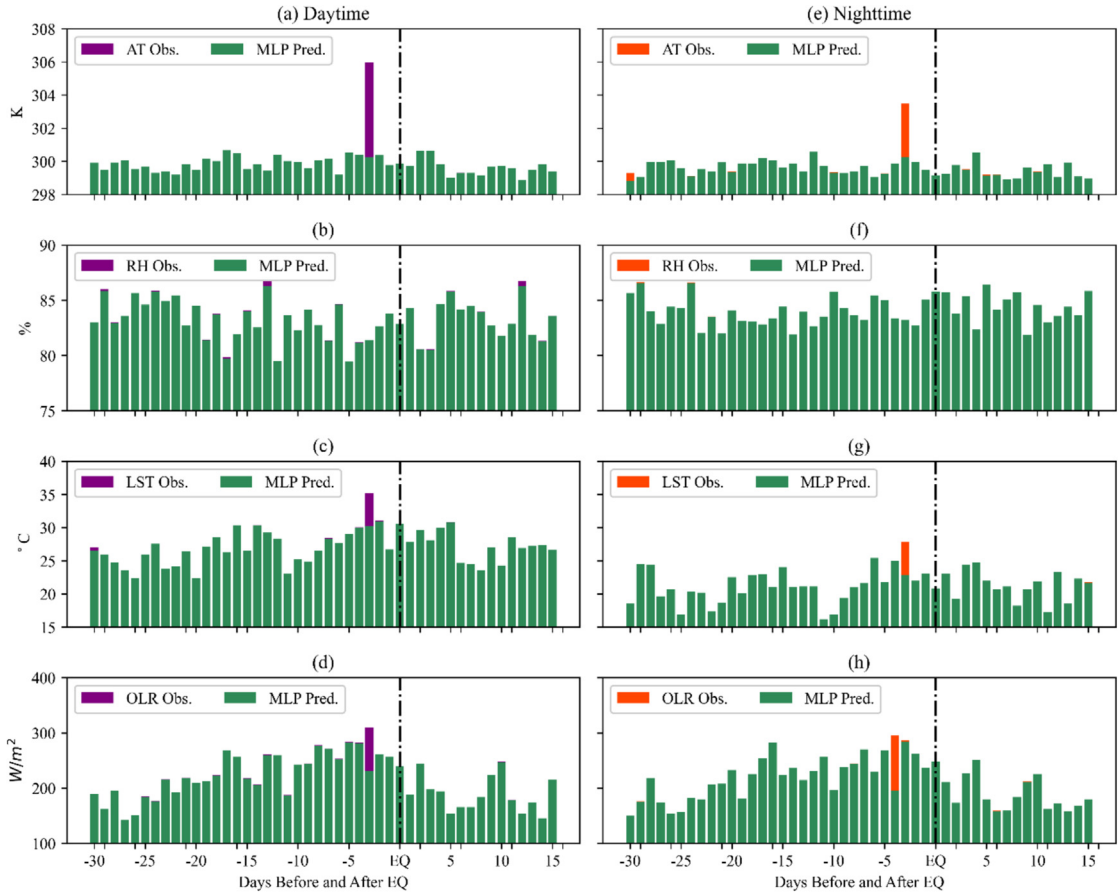

Fig. 5. The illustration of the MLP analysis of daytime and nighttime values. (a) AT daytime data observed and forecasted, (b) RH daytime data observed and forecasted, (c) LST daytime data observed and forecasted, (d) OLR daytime data observed and forecasted, (e) AT daytime data observed and forecasted, (f) RH daytime data observed and forecasted, (g) LST daytime data observed and forecasted, (h) OLR daytime data observed and forecasted. The black dashed line is for the EQ-day.

of earthquakes on the Earth's atmosphere. After noticing the promising results, we can conclude that earthquakes can cause severe variations in the atmosphere alone. The precursors became evident in various parameters within three days prior to the main shock at the instance of more precursory signals of varying magnitudes near the main shock day. The outcomes of these analyses unveil notable atmospheric variations attributed to the Philippines EQ after the previous multi-parametric approach of De Santis et al. (2022). They correlated multiple parameters and found significant evidences to future main shock in a sequence from lithosphere to atmosphere and ionosphere by incorporating various satellites values. However, the precursors were also analyzed using various ML as well as descriptive statistics approaches before the main shock of an upcoming event (Akhoondzadeh, 2012a, Adil et al., 2021b; Freund, 1997; Nekoee and Shah-Hosseini, 2020; Shah et al., 2023a,b; Shahzad et al., 2023; Qasim et al., 2023; Shah et al., 2020). In this paper, we also followed the same trend of previous multi-parametric approach for the future main shock with the addition of ML approach to clear the significant precursors before and after the main shock (Lv et al., 2024; Shi et al., 2024; Wang et al., 2024). However, the ML methods are used only to justify the anomalous atmospheric values rather than an isolated approach for precursory delineation. One can see clearly the anomalies in time series with descriptive statistical methods and ML approaches associated with the main shock to provide an integrated value beyond the bounds (Hu and Sugiyama, 2025). Before this study, Khalid et al. (2024) detected significant surface and atmospheric anomalies through a comprehensive multi-parametric analysis by incorporating various remotely sensed atmospheric observables in statistical and ML methodologies of the Mw > 6.0 EQs in the USA in 2019 and 2020. They indicated a cascade of events potentially triggered by the primary seismic shock. Moreover, they showed a significant increase in all atmospheric variables, with AT rising by 4.9 K and 6.6 K seven and six days before the main shock, respectively. Similarly, they supported their methodologies by NARX analysis to identify a consistent AT anomaly of 5.48 K and 1.86 K occurring three and four days before the main shock using NARX. These findings highlight a distinct variation in the prediction window of AT compared to earlier results (Li et al., 2024; Xie et al., 2024; Han et al., 2022). A notable correlation was also observed between the preceding EQs and changes in AT and RH by indicating a pathway in a coupled interaction within the local

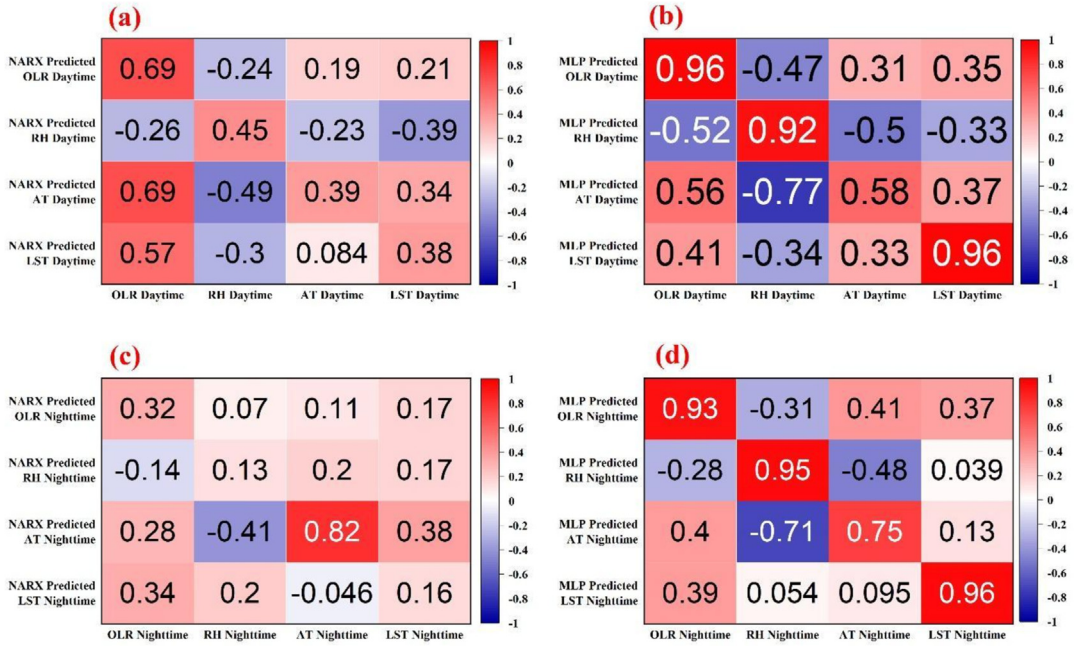

Fig. 6. Correlation graph of the atmospheric parameters; a) correlation between daytime NARX predicted parameters and observed parameters, b) correlation between daytime MLP predicted parameters and observed parameters, c) correlation between nighttime observed atmospheric parameters and NARX predicted parameters, b) correlation between nighttime MLP predicted atmospheric parameters and observed parameters.

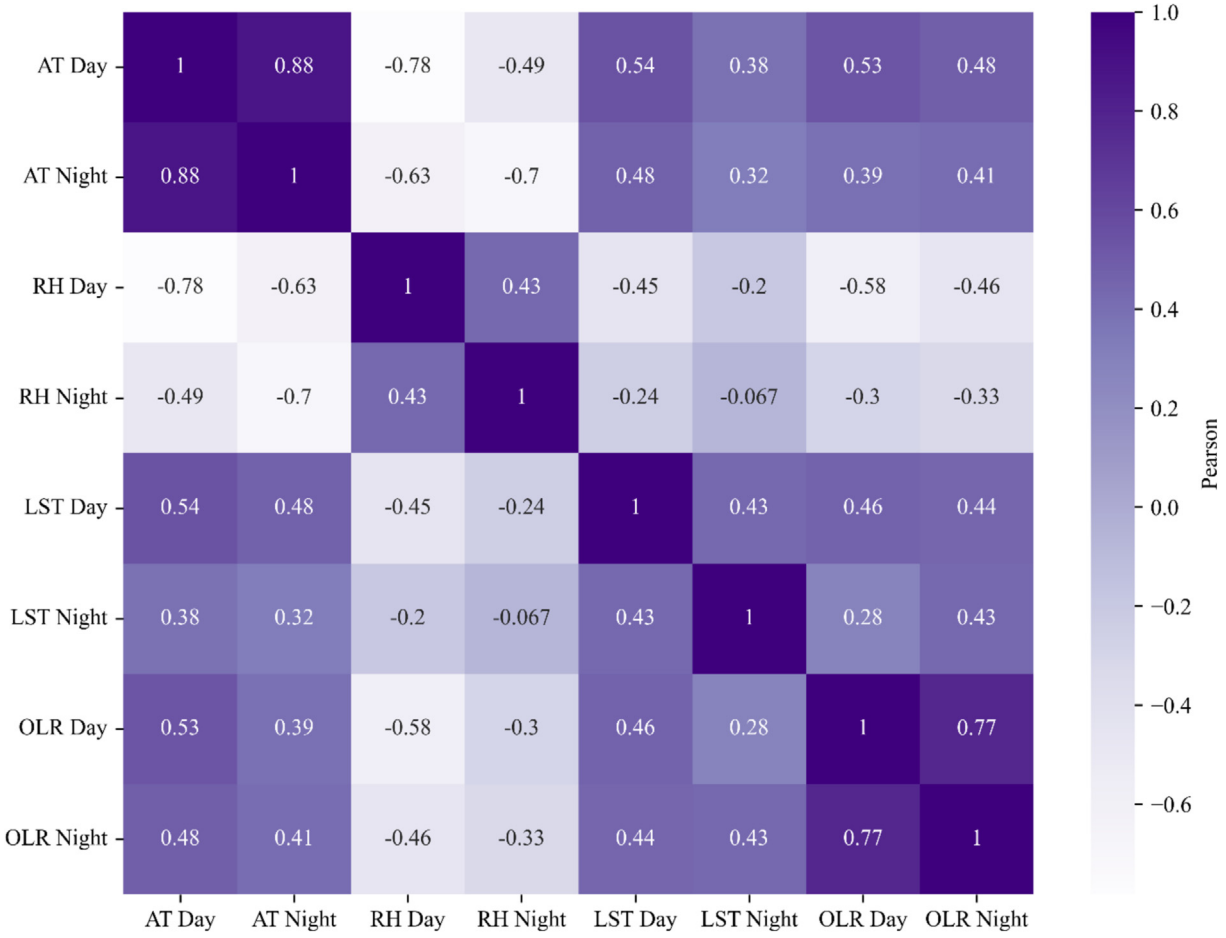

Fig. 7. The Pearson correlation graph between the multiple atmospheric parameters.

Table 1
Illustrates the Statistical method-based anomalies of the Philippines EQ.

Parameters	Pre-EQ	Post-EQ	Deviation fromthe Bounds	Deviation from μ+σ	Deviation from μ+2σ	Deviation from μ+3σ
AT (Daytime)	−3	Nil	4.004 K	5.026 K	4.004 K	2.981 K
AT (Nighttime)	−3	Nil	2.37 K	3.126 K	2.373 K	1.621 K
RH (Daytime)	−3	Nil	−3.04 %	−5.355 %	−3.044 %	−1.035 %
RH (Nighttime)	−3	Nil	−0.9 %	−2.328 %	−0.837 %	−0.652 %
LST (Daytime)	−3	Nil	2.76 °C	5.377 °C	2.767 °C	0.202 °C
LST (Nighttime)	−3	Nil	2.22 °C	3.840 °C	2.222 °C	2.091 °C
OLR (Daytime)	−3	Nil	8.87 W/m^2	52.494 W/m^2	8.876 W/m^2	34.045 W/m^2
OLR (Nighttime)	−3	Nil	3.38 W/m^2	43.742 W/m^2	3.389 W/m^2	36.702 W/m^2

Table 2
Illustrates the NARX based anomalies of Philippines EQ.

Parameters	Pre-EQ	Post-EQ	Deviation from the Bounds
AT (Daytime)	−3	Nil	5.48 K
AT (Nighttime)	−3, −4	Nil	−1.79 K, 1.86 K
RH (Daytime)	−3	Nil	−6.48 %
RH (Nighttime)	−3	Nil	−4.64 %
LST (Daytime)	−3	5	8.75 °C, 6.48 °C
LST (Nighttime)	−3	Nil	7.39 °C
OLR (Daytime)	−3	Nil	62.58 W/m^2
OLR (Nighttime)	−4	Nil	92.25 W/m^2

Table 3
Illustrates the MLP based anomalies of Philippines EQ.

Parameters	Pre-EQ	Post-EQ	Deviation from the Bounds
AT (Daytime)	−3	Nil	5.71 K
AT (Nighttime)	−3	Nil	3.22 K
RH (Daytime)	−3	Nil	−5.797 %
RH (Nighttime)	−3	Nil	−2.96 %
LST (Daytime)	−3	Nil	4.92 °C
LST (Nighttime)	−3	Nil	5.01 °C
OLR (Daytime)	−3	Nil	79.54 W/m^2
OLR (Nighttime)	−4	Nil	100.34 W/m^2

atmospheric system over the epicenter (Draz et al., 2023; Sun et al., 2024a; Guo et al, 2024; Wang et al., 2023). Furthermore, this study offered a more comprehensive examination of the constraints associated with the previous studies employing machine learning techniques to identify suitable atmospheric precursors across different atmospheric layers.

In our observations, a notable increment in MODIS LST is noticed for both the daytime and nighttime in the Figs. 3–5 in just three days prior the major event. The increase is 4.92 °C during the daytime and 5.01 °C during the nighttime predicted by MLP. The tectonic pressures within the Dobrovolsky region may increase the LST owing to the emission of diverse greenhouse gases and radon into the atmosphere (Hafeez et al., 2022; Qasim et al., 2024). There is also a potential for p-hole carriers to contribute to LST anomalies linked to EQs by experiencing intense tectonic stress on crustal rocks (Qasim et al., 2024; Freund, 2011). We also observed a substantial rise in OLR datasets during both the daytime and nighttime for this Philippines EQ analyzed in Figs. 3–5. This increase is due to the energy amalgamation resulting from EQs in the earth atmosphere, leading to heat anomalies caused by gas emission from the epicenter (Khalid et al., 2024; Shah et al., 2021; Shah et al., 2024; Xie et al., 2022; Cao et al., 2024). Our study alsoobserved this phenomenon and additionally identified a significant increase in OLR following the sudden release of EQ energy just before the major event. The previous reports also presented many precursors methods for detection before and after the main shock (Wang et al., 2024; Gao et al., 2023). Moreover, it is also proposed that the OLR variations are induced by a change in seismic tectonic stress, impacting the physical behavior of the underlying surface radiation (Khalid et al., 2024; Su et al., 2021). In this study, we uncovered the indicators for future events using multilayer and multimode satellite data, employing enhanced statistical and ML techniques. There are clear indicators of abnormalities in all possible earthquake precursors within the Dobrovolsky region emerge over a period of three to five days and also provides a thorough explanation of the emergence, synchronization, and correlation among these short-term anomalies.

Furthermore, other apparent markers for anomaly identification in this investigation are the Pearson correlation between the observed values and trained data of ML offers an additional confirmation of seismic energy transmission within the system over the seismic preparation period. We noticed prominent anomalies as possible precursors in the context of Mw 7.0 Philippines EQ. These anomalies offered a clear understanding for further studies to aid the development in lithosphere-atmosphere coupling hypothesis.

6. Conclusions

In this paper, we have observed simultaneous succession in the atmosphere indices as remotely sensed missions for the Mw 7.0 Philippines EQ. The primary findings are listed below.

1) We noticed notable positive and negative variations within a 5-day window in both the statistical methods and ML techniques.

2) The unusual changes observed in OLR, LST, AT, and RH support the connection between EQs and the atmosphere as proposed by the LAIC hypothesis.
3) The sharp decrease in RH, as determined by Statistical, NARX and MLP methods, revealing declines of −3.04 %, −6.48 %, and −5.979 % during daytime, and −0.9 %, −4.64 %, and −2.96 % during nighttime, suggested the cooling effect of hot gases originating from seismic areas within the LAIC.
4) There is also a notable rise in AT as determined through Statistical, NARX, and MLP techniques with increase of 4.004 K, 5.48 K, and 5.71 K during daytime, and 2.37 K, 1.86 K, 3.22 K during nighttime. Similarly, OLR exhibited increases of 8.87 W/m^2, 62.58 W/m^2, and 79.54 W/m^2 during daytime, and 3.38 W/m^2, 92.25 W/m^2, and 100.34 W/m^2 during nighttime. Additionally, LST increases by 2.76 °C, 8.75 °C, and 4.92 °C during daytime, and 2.22 °C, 7.39 °C, 5.01 °C during nighttime.
5) Through the analysis of multi-parameter data using diverse techniques, we were able to ascertain the precursory characteristics of various parameters in relation to the EQ.

In conclusion, with the aim of improving EQ forecasting accuracy and understanding of earthquake precursors, further research should prioritize using higher-resolution data, exploring multiple variables, and demonstrating more effective prediction frameworks.

Declaration of competing interest

The authors declare that they have no known competing financial interests or personal relationships that could have appeared to influence the work reported in this paper.

Acknowledgements

The authors express their gratitude to USGS community for making earthquake information data available. We are extremely grateful to NASA for their provision of MODIS data and other atmospheric parameters data. Punyawi Jamjareegulgarn acknowledged the financial support for this research from Fundamental Fund (FF68) of the Thailand Science Research and Innovation Fund (Grant Number: RE-KRIS/FF68/84). The authors extend their appreciation to King Saud University for funding this work through Researchers Supporting Project number (RSP2025R133), King Saud University, Riyadh, Saudi Arabia.

References

Adil, M.A., Şentürk, E., Pulinets, S.A., Amory-Mazaudier, C., 2021a. A Lithosphere–Atmosphere–Ionosphere Coupling Phenomenon Observed Before M 7.7 Jamaica Earthquake. Pure Appl. Geophys. 178, 3869–3886. https://doi.org/10.1007/s00024-021-02867-z.

Adil, M.A., Şentürk, E., Shah, M., Naqvi, N.A., Saqib, M., Abbasi, A.R., 2021b. Atmospheric and ionospheric disturbances associated with the M> 6 earthquakes in the East Asian sector: A case study of two consecutive earthquakes in Taiwan. J. Asian Earth Sci. 220. 104918. https://doi.org/10.1016/j.jseaes.2021.104918.

Akhoondzadeh, M., 2013a. (2013a), A comparison of classical and intelligent methods to detect potential thermal anomalies before the 11 August 2012 Varzeghan, Iran. Earthquake, Natural Hazards and Earth System Sciences 13, 1077–1083. https://doi.org/10.5194/nhess-13-1077-2013.

Akhoondzadeh, M., 2013b. A MLP neural network as an investigator of TEC time series to detect seismo-ionospheric anomalies. Adv. Space Res. 51, 2048–2057. https://doi.org/10.1016/j.asr.2013.01.012.

Blackett, M., Wooster, M.J., Malamud, B.D., 2011. Exploring land surface temperature earthquake precursors: A focus on the Gujarat (India) earthquake of 2001. Geophys. Res. Lett. Solid Earth 38, 2011. https://doi.org/10.1029/2011GL048282.

Cao, Y., Xie, Z., Li, W., et al., 2024. Combined Path Following and Direct Yaw-Moment Control for Unmanned Electric Vehicles Based on Event-Triggered T–S Fuzzy Method. Int. J. Fuzzy Syst. 26, 2433–2448. https://doi.org/10.1007/s40815-024-01717-z.

Carter, B., Kellerman, A.C., Kane, T., Dyson, P., Norman, R., Zhang, K., 2013. Ionospheric precursors to large earthquakes: A case study of the 2011 Japanese Tohoku Earthquake. J. Atmos. Sol. Terr. Phys. 102, 290–297. https://doi.org/10.1016/j.jastp.2013.06.006.

Chen, J., Song, Y., Li, D., Lin, X., Zhou, S., Xu, W., 2024. Specular Removal of Industrial Metal Objects Without Changing Lighting Configuration. IEEE Trans. Ind. Inf. 20 (3), 3144–3153. https://doi.org/10.1109/TII.2023.3297613.

D'Alessandro, A., Scudero, S., Siino, M., Alessandro, G., Mineo, R.J., 2020. Long-term monitoring and characterization of soil radon emission in a seismically active area. Geochem., Geophys., Geosyst. 21. e2020GC009061. https://doi.org/10.1029/2020GC009061.

De Santis, A., Perrone, L., Calcara, M., Campuzano, S.A., Cianchini, G., D'Arcangelo, S., Di Mauro, D., Marchetti, D., Nardi, A., Orlando, M., Piscini, A., Sabbagh, D., Soldani, M., 2022. Multiparametric and multilayer study of June 15, 2019 M7.2 Kermadec Islands earthquake. Remote Sensing of Environment 283. 113325. https://doi.org/10.1016/j.rse.2022.113325.

Deb, A., Gazi, M., Barman, C., 2016. Anomalous soil radon fluctuations–signal of earthquakes in Nepal and eastern India regions. J. Earth Syst. Sci. 125, 1657–1665. https://doi.org/10.1007/s12040-016-0757-z.

Dobrovolsky, I., Zubkov, S., Miachkin, V.J.P., 1979. Estimation of the size of earthquake preparation zones. Pure Appl. Geophys. 117, 1025–1044. https://doi.org/10.1007/BF00876083.

Draz, M.U., Shah, M., Jamjareegulgarn, P., Shahzad, R., Hasan, A.M., Ghamry, N.A., 2023. Deep machine learning based possible atmospheric and Ionospheric precursors of the 2021 Mw 7.1 Japan earthquake. Remote Sensing (Basel) 15, 1904. https://doi.org/10.3390/rs15071904.

Du, W., Wang, G., 2014. Fully probabilistic seismic displacement analysis of spatially distributed slopes using spatially correlated vector intensity measures. Earthq. Eng. Struct. Dyn. 43 (5), 661–679. https://doi.org/10.1002/eqe.2365.

Eshkuvatov, H., Ahmedov, B., Shah, M., Begmatove, D., Jamjareegulgarn, P., Morales, A.M., 2024. Exploring electromagnetic wave propagation through the ionosphere over seismic active zones. Pure Appl. Geophys. https://doi.org/10.1007/s00024-024-03532-x.

Freund, F., 1997. Pre-earthquake signals: Underlying physical processes. J. Asian Earth Sci. 41, 383–400. https://doi.org/10.1016/j.jseaes.2010.03.009.

Freund, F., Ouillon, G., Scoville, J., Sornette, D., 2021. Earthquake precursors in the light of peroxy defects theory: Critical review of systematic observations. Eur. Phys. J. Spec. Top. 230, 7–46. https://doi.org/10.1140/epjst/e2020-000243-x.

Gao, X., Dai, Y., Zhang, C., Zhang, Y., Zong, W., Zhang, W., Chen, R., Zhu, J., Hu, X., Wang, M., Chen, R., Du, Z., Guo, F., Dong, H., Liu, Y., He, H., Zhao, S., Zhao, F., Li, J., Parkin, I.P., Carmalt, C.J., He,

G., 2023. When It's Heavier: Interfacial and Solvation Chemistry of Isotopes in Aqueous Electrolytes for Zn-ion Batteries. Angewandte Chemie (International Ed. in English), 62. https://doi.org/10.1002/anie.202300608.

Geller, R., 1997. Earthquake prediction: a critical review. Geophys. J. Int. 131 (3), 425–450. https://doi.org/10.1111/j.1365-246X.1997.tb06588.x.

Guo, S., Deng, B., Chen, C., Ke, J., Wang, J., Long, S., Xu, K., 2024. Seeking in ride-on-demand service: a reinforcement learning model with dynamic price prediction. IEEE Internet Things J. 11, 29890–29910. https://doi.org/10.1109/JIOT.2024.3407119.

Hafeez, A., Shah, M., Ehsan, M., et al., 2021. Possible atmosphere and ionospheric anomalies of the 2019 pakistan earthquake using statistical and machine learning procedures on MODIS LST, GPS TEC, and GIM TEC. IEEE J. Sel. Top. Appl. Earth Obs. Remote Sens. 14, 11126–11133. https://doi.org/10.1109/JSTARS.2021.3119382.

Hafeez, A., Ehsan, M., Abbas, A., Shah, M., Shahzad, R., 2022. Machine learning-based thermal anomalies detection from MODIS LST associated with the Mw 7.7 Awaran, Pakistan earthquake. Nat. Hazards, 1–19. https://doi.org/10.1007/s11069-021-05131-8.

Han, D., Zhu, Y., Li, D., Liang, W., Souri, A., Li, K., 2022. A blockchain-based auditable access control system for private data in service-centric IoT environments. *IEEE Trans. Ind. Inf.* 18, 3530–3540. https://doi.org/10.1109/TII.2021.3114621.

Heki, K., 2011. Ionospheric electron enhancement preceding the 2011 Tohoku-Oki earthquake. Geophysical Research Letter 38. https://doi.org/10.1029/2011GL047908.

Hu, Y., Sugiyama, Y., 2025. Well-posedness of the initial-boundary value problem for 1D degenerate quasilinear wave equations. Advances in Differential Equations. 30 (3/4), 177–206. https://doi.org/10.57262/ade030-0304-177.

Jiao, Z., Shan, X., 2022. Pre-seismic temporal integrated anomalies from multiparametric remote sensing data. Remote. Sens. 14, 2343.

Khalid, Z., Shah, M., Riaz, S., Ghaffar, B., Jamjareegulgarn, P., 2024. Atmospheric precursors associated with two Mw > 6.0 earthquakes using machine learning methods. Nat. Hazards. https://doi.org/10.1007/s11069-024-06562-9.

Khan, M.M., Ghaffar, B., Shahzad, R., Khan, M.R., Shah, M., Amin, A. H., Eldin, S.M., Naqvi, N.A., Ali, R., 2022. Atmospheric Anomalies Associated with the 2021 M_w 7.2 Haiti Earthquake Using Machine Learning from Multiple Satellites. Sustainability 14, 14782. https://doi.org/10.3390/su142214782.

Kuo, C.L., Lee, L., Huba, J.D., 2014. An improved coupling model for the lithosphere-atmosphere-ionosphere system. *J. Geophys. Res. Space Phys.* 119, 3189–3205.

Li, Y.Z., Li, J., Feng, C., Wen, M., Zhang, Y., 2024. An interface constitutive model of plastic tensile–compressive damage under impact loading based on continuous–discontinuous framework. Comput. Geotech. https://doi.org/10.1016/j.compgeo.2024.106502.

Liu, J., Chuo, Y.J., Shan, S.J., Tsai, Y.B., Chen, Y., Pulinets, S.A., Yu, S. B., 2004. Pre-earthquake ionospheric anomalies registered by continuous GPS TEC measurements. Ann. Geophys. 22, 1585–1593.

Liu, J., Xie, Z., Gao, J., Hu, Y., Zhao, J., 2021. Failure characteristics of the active-passive damping in the functionally graded piezoelectric layers-magnetorheological elastomer sandwich structure. International Journal of Mechanical Sciences. https://doi.org/10.1016/j.ijmecsci.2021.106944.

Lv, H., Zeng, J., Zhu, Z., Dong, S., Li, W., 2024. Study on prestress distribution and structural performance of heptagonal six-five-strut alternated cable dome with inner hole. Structures. https://doi.org/10.1016/j.istruc.2024.106724.

Ma, K., Peng, Y., Liao, Z., Wang, Z., 2024. Dynamic responses and failure characteristics of the tunnel caused by rockburst: An entire process modelling from incubation to occurrence phases. Comput. Geotech. 171. 106340. https://doi.org/10.1016/j.compgeo.2024.106340.

Nekoee, M., Shah-Hosseini, R., 2020. Thermal anomaly detection using NARX neural network method to estimate the earthquake occurrence time. Earth Observation and Geomatics Engineering 4 (2), 98–108. https://doi.org/10.22059/eoge.2021.292253.1067.

Ouzounov, D., Freund, F., 2004. Mid-infrared emission prior to strong earthquakes analyzed by remote sensing data. *Adv. Space Res.* 33, 268–273.

Pulinets, S.A., Dunajecka, M.A., 2007. Specific variations of air temperature and relative humidity around the time of Michoacan earthquake M8.1 Sept. 19, 1985 as a possible indicator of interaction between tectonic plates. *Tectonophysics* 431, 221–230.

Pulinets, S.A., Ouzounov, D., 2011. Lithosphere-Atmosphere-Ionosphere Coupling (LAIC) Model - An Unified Concept for Earthquake Precursors Validation. J. Asian Earth Sci. 41, 371–382.

Qasim, M., Shah, M., Shahzad, R., Jamjareegulgarn, P., 2023. Atmospheric precursors from multiple satellites associated with the 2020 Mw 6.5 Idaho (USA) earthquake, Advances in Space Research, https://doi.org/10.1016/j.asr.2023.09.057.

Salikhov, N., Shepetov, A., Pak, G., Nurakynov, S., Ryabov, V., Saduyev, N., Sadykov, T., Zhantayev, Z., Zhukov, V., 2022. Monitoring of Gamma Radiation Prior to Earthquakes in a Study of Lithosphere-Atmosphere-Ionosphere Coupling in Northern Tien Shan. *Atmos.* 13 (1667), 2022. https://doi.org/10.3390/atmos13101667.

Shah, M., Jin, S.G., 2015. Statistical characteristics of seismo-ionospheric GPS TEC disturbances prior to global Mw≥ 5.0 earthquakes (1998-2014). J. Geodyn. 92, 42–49. https://doi.org/10.1016/j.jog.2015.10.002.

Shah, M., Draz, M.U., Saleem, T., 2023a. A comprehensive study on the synchronized outgoing longwave radiation and relative humidity anomalies related to global Mw≥6.5 earthquakes. Nat. Hazards. https://doi.org/10.1007/s11069-023-06262-w.

Shah, M., Calabia, A., Tariq, M. A., Ahmed, J., Ahmed, A., 2020. Possible ionosphere and atmosphere precursory analysis related to Mw >6.0 earthquakes in Japan. Remote Sens. Environ. 239 (2020), 111620, https://doi.org/10.1016/j.rse.2019.111620.

Shah, M., Ehsan, M., Abbas, A., A. Ahmed and Jamjareegulgarn, P., 2021, Possible Thermal Anomalies Associated with Global Terrestrial Earthquakes During 2000-2019 Based on MODIS-LST, IEEE Geoscience and Remote Sensing Letters vol. 19, pp. 1-5, 2022, Art no. 1002705, https://doi.org/10.1109/LGRS.2021.3084930.

Shah, M., Abbas, A., Adil, M.A., Ehsan, M., Ashraf, U., Júnior J. F. O., Tariq, M. A., Ahmed, J., Ali, A., 2022, Possible seismo-ionospheric anomalies associated with Mw > 5.0 earthquakes during 2000-2020 from GNSS TEC, Advances in Space Research, https://doi.org/10.1016/j.asr.2022.04.025.

Shah, M., Jin, S.G., 2018. Pre-seismic ionospheric anomalies of the 2013 Mw=7.7 Pakistan earthquake from GPS and COSMIC observations. Geod. Geodyn. https://doi.org/10.1016/j.geog.2017.11.008.

Shah, M., Shahzad, R., Ehsan, M., Ghaffar, B., Ullah, I., Jamjareegulgarn, P., Hassan, A.M., 2023b. Seismo Ionospheric Anomalies around and over the Epicenters of Pakistan Earthquakes. Atmos. 14 (3), 601. https://doi.org/10.3390/atmos14030601.

Shahzad, F., Shah, M., Riaz, S., Ghaffar, B., Ullah, I., Eldin, S.M., 2023. Integrated Analysis of LithosphereAtmosphere-Ionospheric Coupling Associated with the 2021 Mw 7.2 Haiti Earthquake. Atmos. 14, 347. https://doi.org/10.3390/atmos14020347.

Shi, J., Han, D., Chen, C., et al. KTMN, 2024. Knowledge-driven Two-stage Modulation Network for visual question answering. Multimedia Systems 30, 350. https://doi.org/10.1007/s00530-024-01568-6.

Su, B., Li, H., Ma, W., Jing, Z., Qi, Y., Jing, C., Yue, C., Kang, C., 2021. The outgoing longwave radiation analysis of medium and strong earthquakes. *IEEE J. Sel. Top. Appl. Earth Obs. Remote Sens.* 14, 6962–6973.

Sun, Z., Elsworth, D., Cui, G., Li, Y., Zhu, A., Chen, T., 2024. Impacts of rate of change in effective stress and inertial effects on fault slip behavior: new insights into injection-induced earthquakes. J. Geophys. Res. Solid Earth 129 (2). e2023JB027126. https://doi.org/10.1029/2023JB027126.

Sun, X., Zhang, K., Liu, Q., Bao, M., Chen, Y., 2024a. Harnessing domain insights: A prompt knowledge tuning method for aspect-based sentiment analysis. Knowl. Based Syst. 298. 111975. https://doi.org/10.1016/j.knosys.2024.111975.

Tian, H., Huang, N., Niu, Z., Qin, Y., Pei, J., Wang, J., 2019. Mapping winter crops in china with multi-source satellite imagery and phenology-based algorithm. *Remote. Sens.* 11, 820.

Tian, Y., Zhao, Y., Son, S., Luo, J., Oh, S., Wang, Y., 2023. A deep-learning ensemble method to detect atmospheric rivers and its application to projected changes in precipitation regime. J. Geophys. Res. Atmos. 128 (12). e2022JD037041. https://doi.org/10.1029/2022JD037041.

Tian, Y., Zhao, Y., Li, J., Xu, H., Zhang, C., Deng, L., Peng, M., 2024. Improving CMIP6 atmospheric river precipitation estimation by cycle-consistent generative adversarial networks. J. Geophys. Res. Atmos. 129 (14). e2023JD040698. https://doi.org/10.1029/2023JD040698.

Wang, J., Ji, J., Jiang, Z., Sun, L., 2023. Traffic flow prediction based on spatiotemporal potential energy fields. IEEE Trans. Knowl. Data Eng. 35, 9073–9087. https://doi.org/10.1109/TKDE.2022.3221183.

Wang, Z., Liao, Z., Zhou, B., Yu, G., Luo, W., 2024. SwinURNet: Hybrid Transformer-CNN Architecture for Real-Time Unstructured Road Segmentation. IEEE Transactions on Instrumentation and Measurement 73, 1–16. https://doi.org/10.1109/TIM.2024.3470042.

Wang, Y., Wang, J., Cai, R., Zhang, J., Xia, S., Li, Z., Yu, C., Wu, J., Wang, P., Wu, Y., 2024. Enhanced Local CO Coverage on Cu Quantum Dots for Boosting Electrocatalytic CO2 Reduction to Ethylene. Advanced Functional Materials.

Xie, D., Huang, H., Feng, L., Sharma, R.P., Chen, Q., Liu, Q., Fu, L., 2023a. Aboveground biomass prediction of arid shrub-dominated community based on airborne LiDAR through parametric and nonparametric methods. Remote Sens. (Basel) 15 (13), 3344. https://doi.org/10.3390/rs15133344.

Xie, J., Wen, M., Ding, P., Tu, Y., Wu, D., Liu, K., Tang, K., Chen, M., 2024. One-dimensional consolidation analysis of layered unsaturated soils: An improved model integrating interfacial flow and air contact resistance effects. *Comput. Geotech.*. https://doi.org/10.1016/j.compgeo.2024.106791.

Xie, Z., You, W., Wong, P.K., Li, W., Zhao, J., 2022. Fuzzy robust non-fragile control for nonlinear active suspension systems with time varying actuator delay. Proceedings of the Institution of Mechanical Engineers, Part D: Journal of Automobile Engineering 238, 46–62. https://doi.org/10.1177/09544070221125528.

Xu, H., Li, Q., Chen, J., 2022. Highlight Removal from A Single Grayscale Image Using Attentive GAN. Appl. Artif. Intell. 36 (1). 1988441. https://doi.org/10.1080/08839514.2021.1988441.

Zhang, Z., Xu, Y., Song, J., Zhou, Q., Rasol, J., Ma, L., 2023a. Planet craters detection based on unsupervised domain adaptation. IEEE Trans. Aerosp. Electron. Syst. 59 (5), 7140–7152. https://doi.org/10.1109/TAES.2023.3285512.

Zhao, Y., Wang, X., Huang, Z., 2024. Multi-function radar modeling: a review. IEEE Sens. J. https://doi.org/10.1109/JSEN.2024.3436877.

Zhao, Y., Li, J., Tian, Y., Li, J., 2024a. Distinguish extreme precipitation mechanisms associated with atmospheric river and non-atmospheric river in the lower yangtze river basin. J. Clim. https://doi.org/10.1175/JCLI-D-23-0400.1.

Zhou, G., Zhao, D., Zhou, X., Xu, C., Liu, Z., Wu, G., Zou, L., 2022a. An RF Amplifier Circuit for Enhancement of Echo Signal Detection in Bathymetric LiDAR. IEEE Sens. J. 22 (21), 20612–20625. https://doi.org/10.1109/JSEN.2022.3206763.

Zhou, G., Zhou, X., Chen, J., Jia, G., Zhu, Q., 2022b. LiDAR echo gaussian decomposition algorithm for FPGA implementation. Sensors 22 (12), 4628. https://doi.org/10.3390/s22124628.

Zhu, X., Xu, Z., Liu, Z., Liu, M., Yin, Z., Yin, L., Zheng, W., 2022. Impact of dam construction on precipitation: a regional perspective. Mar. Freshw. Res. https://doi.org/10.1071/MF22135.